

**A Defective Thesis: Studying the Behaviour of Defects in
Liquid-Crystalline Materials**

by

A. A. S. Green

B.Sc., University of Calgary 2011

M.S., University of Colorado at Boulder 2015

A thesis submitted to the
Faculty of the Graduate School of the
University of Colorado in partial fulfillment
of the requirements for the degree of
Doctor of Philosophy
Department of Physics
2019

This thesis entitled:
A Defective Thesis: Studying the Behaviour of Defects in Liquid-Crystalline Materials
written by A. A. S. Green
has been approved for the Department of Physics

Prof. Noel Clark

Who knows

Please, someone

Date _____

The final copy of this thesis has been examined by the signatories, and we find that both the content and the form meet acceptable presentation standards of scholarly work in the above mentioned discipline.

Green, A. A. S. (Ph.D., Physics)

A Defective Thesis: Studying the Behaviour of Defects in Liquid-Crystalline Materials

Thesis directed by Prof. Noel Clark

Often the abstract will be long enough to require more than one page, in which case the macro “\OnePageChapter” should *not* be used.

But this one isn’t, so it should.

Dedication

To all of the fluffy kitties.

Acknowledgements

Here's where you acknowledge folks who helped. But keep it short, i.e., no more than one page, as required by the Grad School Specifications.

Contents

Chapter

1	Introduction	1
1.1	Liquid Crystals	1
1.1.1	Phases of matter	1
1.1.2	The Rod Liquid Crystal	1
1.1.3	The Bent Liquid Crystal	1
1.1.4	Characterization of Liquid Crystals: Case Study	1
1.2	Fluid Dynamics	1
1.3	Fluid Dynamics of Liquid Crystals	1
2	The Discovery of Helicity in Tilted Bent-Core Smectics: $\text{Sm}(\text{CP})_\alpha$	2
2.1	A Brief History of Chirality in Bent-Core Smectics	2
2.1.1	Conventional Phase of PAL30	2
2.2	Characteristics of the $\text{Sm}(\text{CP})_\alpha$ phase	4
2.2.1	The PAL30 Molecule and Phases	4
2.2.2	Textures of the $\text{Sm}(\text{CP})_\alpha$ phase	4
2.2.3	Electro-Optic Behaviour of the $\text{Sm}(\text{CP})_\alpha$ phase	8
2.2.4	Freely-Suspended Films of the $\text{Sm}(\text{CP})_\alpha$ phase	10
2.2.5	X-ray Analysis of the $\text{Sm}(\text{CP})_\alpha$ phase	10
2.3	Discussion of the $\text{Sm}(\text{CP})_\alpha$ phase	13

3 chirality on demand: the discovery of activated Chirality in achiral bent-core mesogens	15
3.1 A history of de Vries phases in liquid crystals	15
3.2 Characteristic behaviour of the bent-core de Vries phase	15
3.2.1 Textures of bent-code de Vries phase	15
3.2.2 Electro-optics of bent-core de Vries phase	15
3.2.3 X-ray analysis of bent-core de Vries phase	16
3.3 Discussion for the bent-core de Vries phase	16
4 Metrology Applications of Fluid Crystals	18
4.1 Experimental Design	18
4.2 Theory and Simulation	21
4.3 Results and Discussion	25
Bibliography	28

Appendix

Tables

Table

Figures

Figure

2.1	3
2.2	3
2.3 Textures of the $\text{Sm}(\text{CP})_\alpha$ phase of PAL30: reminiscent of a $\text{SmC}_\text{A}\text{P}_\text{A}$ texture.	4
2.4 Dynamic optical tilt of $\text{Sm}(\text{CP})_\alpha$. On application of a field, the state briefly passes through a ‘dark’ state, where the contrast decreases.	6
2.5 Homeotropic textures of PAL30. The relevant temperatures for the Sm2 phases are 104 °C, and 98 °C. The biaxiality in the Sm2 is distinguished by a small ‘hump’ with small applied field, that gets larger on cooling, and changes in character on cooling through the Sm2→Sm3 phase transition at 99 °C, where it broadens. Reproduced from Sreenilayam et al[20].	7
2.6 Series of polarization current measurements taken in the Sm2 phase of PAL30	9
2.7 Polarization current of Sm2 of PAL30 plotted against applied voltage	9
2.8 SAXS of $\text{Sm}(\text{CP})_\alpha$. The smectic layer size, d , increases monotonically on cooling, with no inflection points that would be characteristic of a untilted→tilted phase transition.	10
2.9 Diffractogram of PAL30 taken in the coexistence region between the $\text{Sm}(\text{CP})_\alpha$ ($q \approx 0.04/\text{\AA}$) and the $\text{SmC}_\text{A}\text{P}_\text{A}$ ($q \approx 0.06/\text{\AA}$).	11

2.10 Temperature behaviour of the $\text{Sm}(\text{CP})_\alpha$ phase plotted as a waterfall plot in (a), and as a contour plot in (b). A bilayer ($d = 112 \text{ \AA} = 2d_0$) corresponds to the 2-layer unit-cell structure of the SmCP_A phase, which sits directly below the $\text{Sm}(\text{CP})_\alpha$ phase in temperature. The resonant peak corresponding to the $\text{Sm}(\text{CP})_\alpha$ phase at $d \approx 150 \text{ \AA}$ is direct evidence that the $\text{Sm}(\text{CP})_\alpha$ phase is not a classic B2-type phase.	12
2.11 X-ray scattering from PAL30. (a) SAXS gives a peak from the smectic layer ordering at $q = q_0$. The RSoXS peak at q_H indicates that there is superlayer orientational ordering with periodicity d_H in the Sm2 phase. In general, superlayer orientational modulation in a smectic generates RSoXS peaks at wavevectors along the layer normal at $q(l, m) = l(2\pi/d_0) \pm m(2\pi/d_H)$ [8]. The observation of an RSoXS reflection at $q = q(0, 1)$ and the absence of an Umklapp peak at $q = q(1, -1)$ in the Sm2 confirms a superlayer helix with a scattering amplitude modulation due to the smectic layering that is undetectably weak. (b) Temperature dependence of resonant scattering. The helix peak at $q_H \approx 1/(2.8d_0)$ becomes diffuse in the Sm3 phase. Splitting of the bilayer peak at q_B , which would indicate helical precession of the bilayer structure, is not observed.	14
3.1	15
3.2	16
3.3	16
3.4	17
3.5	17

- 4.1 Smectic film flow meter geometry. (a) A stainless steel film holder ($45.2\text{ mm} \times 34.8\text{ mm} \times 7.6\text{ mm}$) has a $w = 3.1\text{ mm}$ -wide channel in the form of a racetrack cut to a depth $h = 3.7\text{ mm}$. At viewing ports centered along each ‘arm’, the channel is cut all the way through the film holder (a depth of 7.6 mm). Gas is coupled into and out of the system by means of co-linear, 2 mm -diameter holes at the ends of the film holder. Smectic films are created by coating the bottom of a glass coverslip (the spreader) with liquid crystal material and drawing it across the top opening of the channel. The film is shielded from random air currents from above by a sealed cover (not shown). The photomicrograph shows typical islands (localized regions with more layers than the background film) used to track flow of the film in one of the viewing regions of the racetrack. (b) Schematic cross-section of a smectic film suspended across the channel (not to scale). The film comprises an integer number of smectic layers and can be as thin as two molecules ($\sim 6\text{ nm}$). In general, a meniscus forms where the film contacts the edges of the channel. 19
- 4.2 Analytic analysis of symmetric, two-phase, stratified fluid flow in an infinitely long pipe of width a . (a) Ratio between the average film and air velocities as a function of the phase fraction (the ratio of the volume of the fluid and the volume of the air, $\phi = h_{\text{film}}/h_{\text{air}}$). When the phase fraction is very small, the film is strongly coupled to the air and moves with the same speed. (b) Flow velocity in the top half of the pipe. At left, both air and film are flowing through the pipe (the blue dashed line demarcates the upper boundary of the film), while on the right only air is present. The y dimension is scaled by the half the thickness of the LC film, h_{film} . The flow fields in these two cases are practically indistinguishable, suggesting that the influence of the LC film on the airflow is negligible. 22

- 4.3 Computed airflow in the racetrack geometry. (a) Model velocity field for inlet velocity $v_{\text{inlet}} = 0.15 \text{ m/s}$. The air does not circulate uniformly in the same sense around the racetrack, instead splitting between the front and back legs. (b) Model velocity field for inlet velocity $v_{\text{inlet}} = 0.65 \text{ m/s}$. Above a transition inlet velocity of $v_{\text{inlet}} = 0.55 \text{ m/s}$, the air circulates uniformly around the racetrack. (c) Predicted net film speed ($v_{\text{film}} \propto v_2 - v_1$) for a range of inlet velocities. The slope of this curve gives an average theoretical sensitivity of $S = 0.15$. The background shading reflects the experimental observations with different inlet velocities: for $v_{\text{in}} < 0.3 \text{ m/s}$, the film flow is chaotic; for $0.3 \text{ m/s} < v_{\text{in}} < 1.2 \text{ m/s}$, the film exhibits stable Poiseuille flow; for $v_{\text{in}} > 1.2 \text{ m/s}$, the film undergoes rapid out-of-plane oscillations that make particle tracking impractical. 24
- 4.4 Characterization of flow meter. (a) Velocity profiles over the width of the racetrack channel, with each point corresponding to a specific tracked island. The profiles are well described by parabolas (smooth curves), confirming Poiseuille flow over a wide-range of inlet velocities. At higher velocities, the data are noisier due to the relatively paucity of islands that can be captured in sequential frames. The left-right asymmetry in the number of measurements is an artifact due to defects on one side of the camera sensor. (b) Spatially averaged film velocity in the observation region as a function of inlet air velocity. Measurements were performed over four separate days, using more than 30 films. The volumetric flow rate of the air being injected into the racetrack through the inlet was measured using an independent mechanical sensor. The average film speed is linearly proportional to the speed of the air at the device inlet, with a sensitivity that is independent of flow rate. 26

Chapter 1

Introduction

1.1 Liquid Crystals

1.1.1 Phases of matter

1.1.2 The Rod Liquid Crystal

1.1.3 The Bent Liquid Crystal

1.1.4 Characterization of Liquid Crystals: Case Study

1.2 Fluid Dynamics

1.3 Fluid Dynamics of Liquid Crystals

Chapter 2

The Discovery of Helicity in Tilted Bent-Core Smectics: $\text{Sm}(\text{CP})_\alpha$

The interplay between polarization and chirality has always been front and centre in the development of the banana phases of liquid crystals. From the short-range (bilayer) chiral B2 phases[9], to the long-range helicity of the twist-bend nematic phase, bent-core liquid crystals have been an interesting playground to observe the emergence of spontaneous chirality.

Our discovery of a B2-like phase, with polar, ferrielectric switching that also has a spontaneous twist-bend like helix is the first link between the twist-bend and B2 phases.

2.1 A Brief History of Chirality in Bent-Core Smectics

2.1.1 Conventional Phase of PAL30

To briefly recap Section 1.1.4, the low-temperature phases of PAL30 are conventional B2 phases: the $\text{SmC}_\text{A}P_\text{A}$ and the $\text{SmC}_\text{A}P_\text{F}$. The conventional representation of the polarization current for the Sm3 and Sm4 phases are shown in Figure 2.1.

However, it the switching dynamics of the phases become more clear if the polarization current is plotted directly against the driving voltage, shown in Figure 2.2

This is the end of this section.

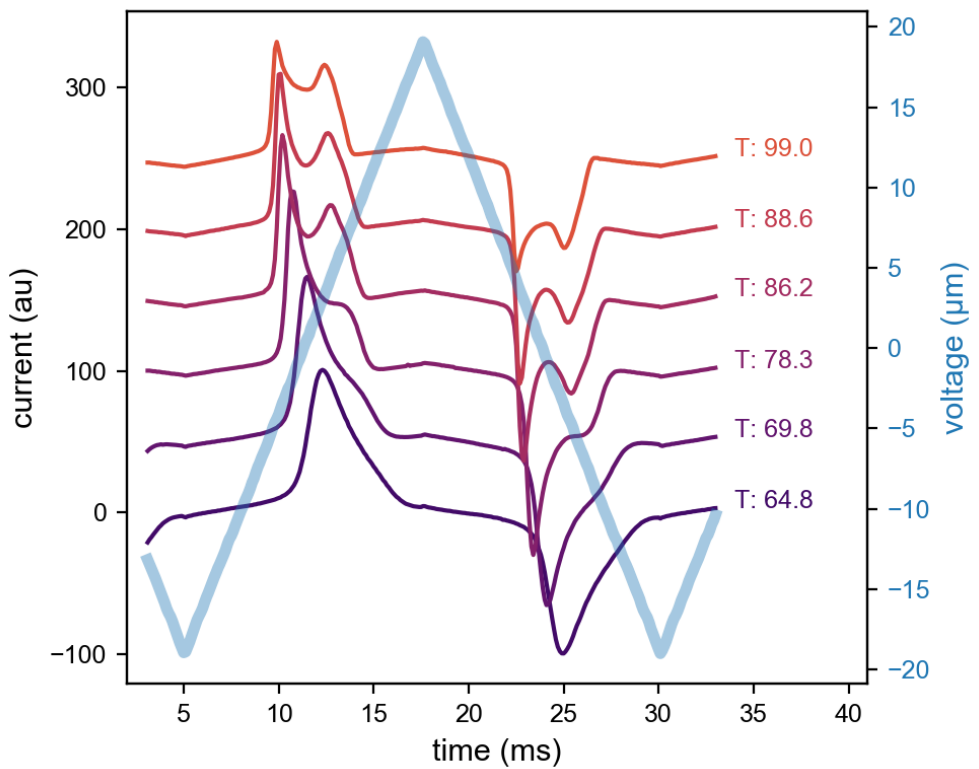


Figure 2.1:

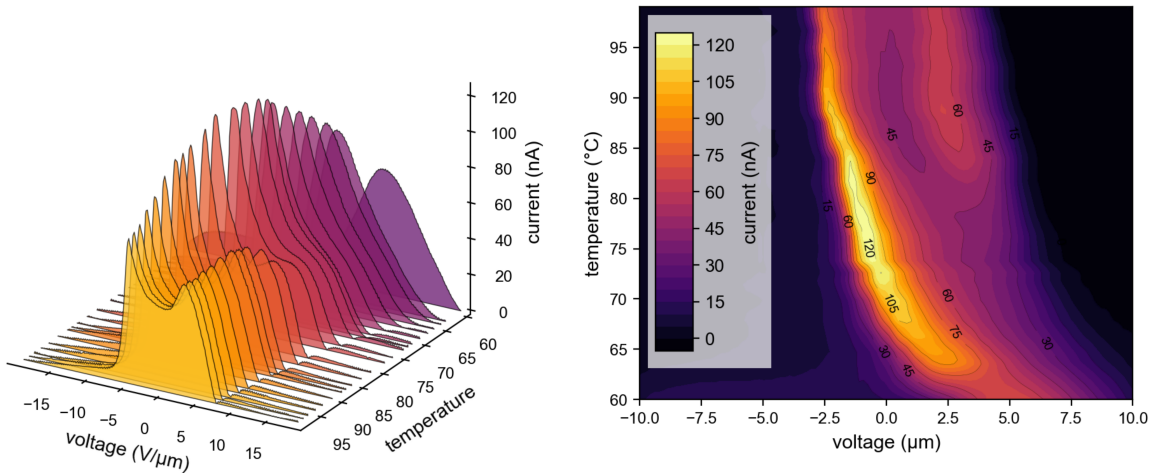


Figure 2.2:

2.2 Characteristics of the $\text{Sm}(\text{CP})_\alpha$ phase

2.2.1 The PAL30 Molecule and Phases

Go bottom up, to get the boring phases out of the way. (maybe put this in the introduction of PAL30)

add phase description with Sm2

2.2.2 Textures of the $\text{Sm}(\text{CP})_\alpha$ phase

2.2.2.1 Planar Aligned Textures

As discussed in Section ??, in planar-aligned cells, the optic axis of the liquid crystal is perpendicular to the \vec{k} of the applied light—meaning we will be sensitive to relative orientations of the long-axis.

In Figure 2.3, the planar textures of the Sm2 phase of PAL30 are shown. Comparing these with previously published textures reveals a strong similarity to the $\text{SmC}_\text{A}\text{P}_\text{A}$ phases[9, 17]. As discussed in Section ??, the PAL30 phase directly below the Sm2 is a $\text{SmC}_\text{A}\text{P}_\text{A}$, but with strikingly long-range and regular conglomerate chiral structure, where the handedness is grouped together into stripes. There exists no clear phase transition in the textures between the Sm2 and Sm3 in planar aligned cells.

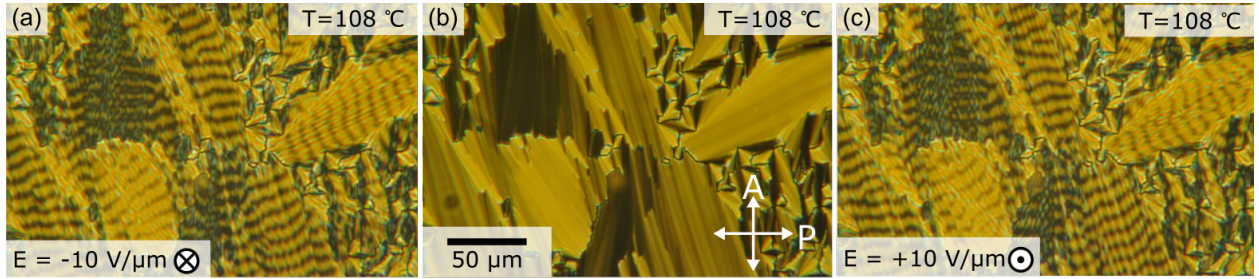


Figure 2.3: Textures of the $\text{Sm}(\text{CP})_\alpha$ phase of PAL30: reminiscent of a $\text{SmC}_\text{A}\text{P}_\text{A}$ texture.

This similarity is due to the fact that, broadly, the $\text{SmC}_\text{A}\text{P}_\text{A}$ and $\text{Sm}(\text{CP})_\alpha$ phases are identical optically. Both phases have unit-cells whose dielectric tensor is uniaxial (where the $\epsilon_{xx} = \epsilon_{yy}$), so

the optic axis will be parallel to the layer normal and the texture appears like a SmA in it's ground state.

Both phases are polar, so with a high enough field both states will switch into an aligned SmC_SP_F state, which gives a birefringent contrast between domains with different handedness. This contrast is because of the synclinic nature of the SmC_SP_F phase— because the tilt is now aligned between the subsequent layers, the phase can organize into conglomerate chiral domains with the optic axis tilted with respect to the layer normal.

We can directly measure the optical tilt in the switched state, by simply rotating the stage when a field has been applied such that an initially dark stripe becomes completely bright. The angle of this rotation is $2\theta_{opt}$. To observe the tilt dynamics, we have to extend this analysis as we cannot rotate a stage at the 20 Hz frequency that these samples usually switch at.

We can extract a measurement of the dynamic optical tilt, θ_{opt} , by examining the contrast between the bright and dark regions of the stripe. Knowing that the brightness of a birefringent material viewed under cross polarizers is $I \propto \sin(2\theta)^2$, the contrast between a “bright” and adjacent “dark” stripe is given by:

$$C = \delta I = I_{\text{bright}} - I_{\text{dark}} = \sin(2\theta_b)^2 - \sin(2\theta_d)^2 \quad (2.1)$$

$$= \frac{1 - \cos(4\theta_b)}{2} - \frac{1 - \cos(4\theta_d)}{2} \quad (2.2)$$

$$= -\sin(2i(\theta_d + \theta_b)) \sin(2(\theta_d - \theta_b)) \quad (2.3)$$

Because of the symmetry of the SmC_SP_F state, we know that $\theta_d = -\theta_b$ (the magnitude of the tilt is equal, but the sign depends on the chirality).

This allows to directly connect the contrast with the tilt angle:

$$C \propto \sin(4\theta_{\text{opt}}). \quad (2.4)$$

This analysis assumes that the state we are measuring can be roughly approximated by a SmC_SP_F. This will be a good approximation at high field strengths, but may be false at lower fields, where the helix of the Sm(CP) _{α} hase may be distorted, but not switched.

figure
describ-
ing this
switching
mecha-
nism

Plotting the result in [Figure 2.4](#) we see thresholdless optical switching, where the contrast (optical tilt) increases linearly with applied field. Interestingly, the $\text{Sm}(\text{CP})_\alpha$ phase accesses a ‘dark’ state, which was also seen in homeotropic cells, shown in [Figure 2.5](#). This will be discussed in further detail in ??

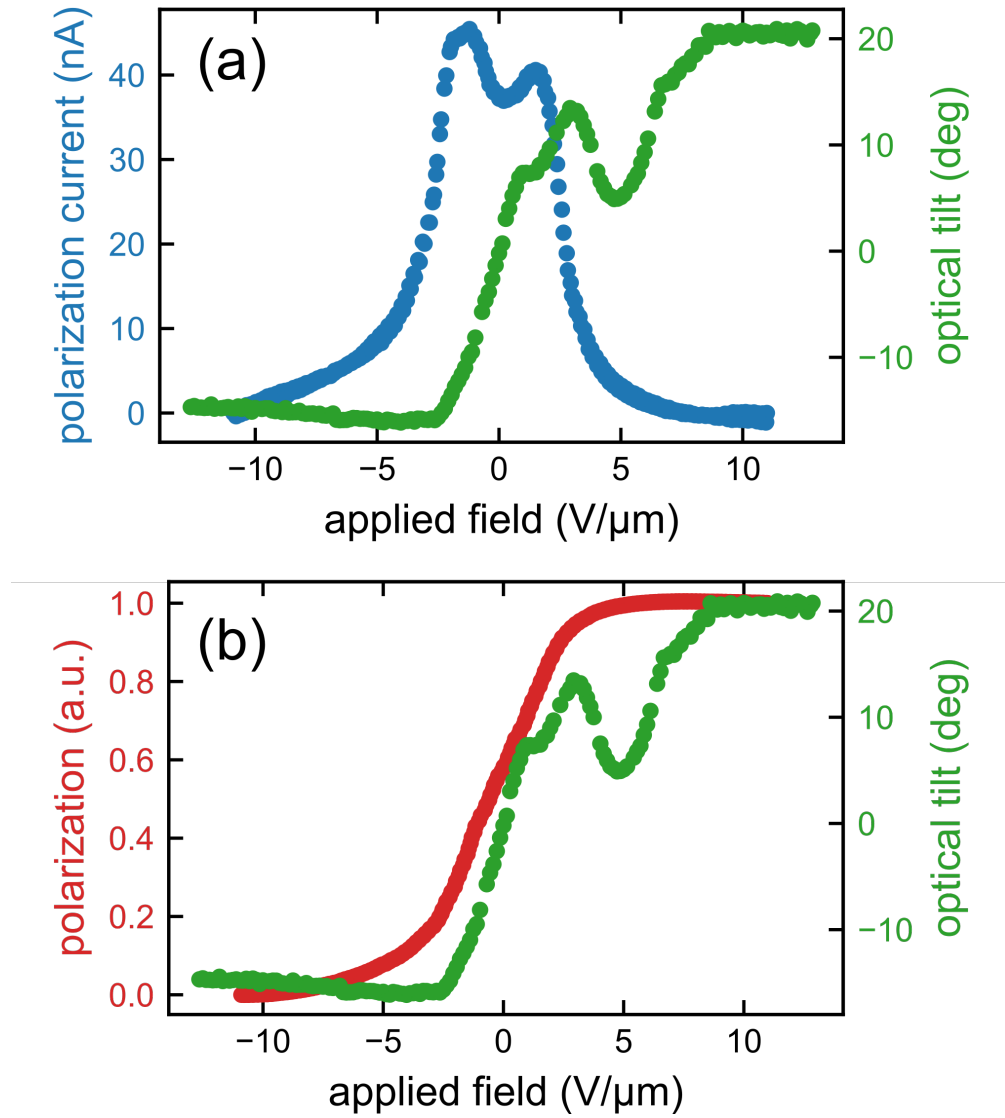
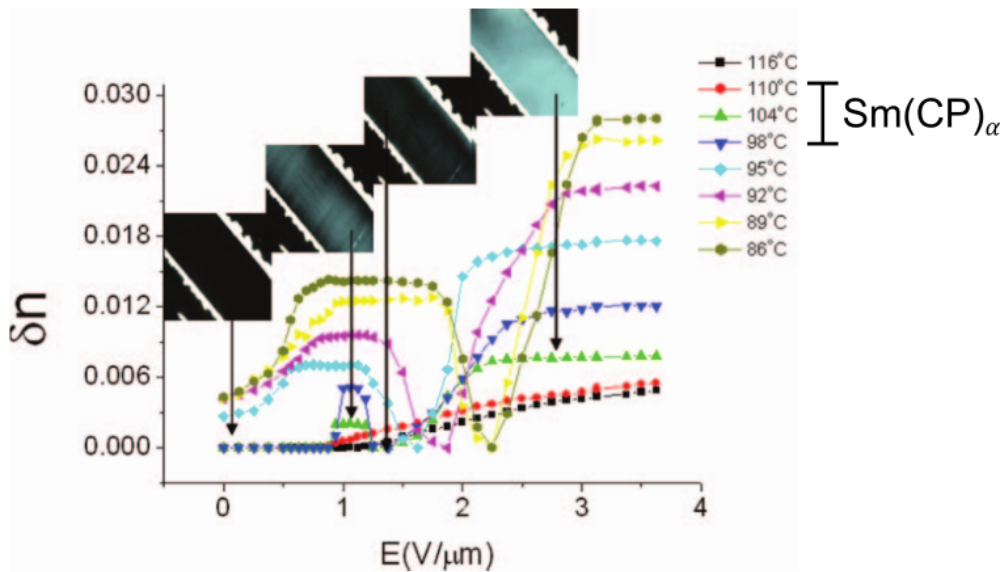


Figure 2.4: Dynamic optical tilt of $\text{Sm}(\text{CP})_\alpha$. On application of a field, the state briefly passes through a ‘dark’ state, where the contrast decreases.

In conclusion, the textures of the $\text{Sm}(\text{CP})_\alpha$ phase have identical characteristics to those of the SmCPA , though an interesting dark state emerges when viewed under dynamic conditions.

2.2.2.2 Homeotropic Aligned Textures

Though we were unable to achieve good homeotropic alignment, we can rely on the published results of the Dublin group, who published a series of papers on the PAL30 homolog series[10, 20, 21, 22]. Though their interpretation is wrong (PAL30 is not an orthogonal phase), they report beautifully aligned homeotropic textures and study the response of these textures to an applied in-plane electric field. These textures are reproduced from Sreenilayam et al[20] in [Figure 2.5](#).



[Figure 2.5](#): Homeotropic textures of PAL30. The relevant temperatures for the Sm2 phases are 104 °C, and 98 °C. The biaxiality in the Sm2 is distinguished by a small ‘hump’ with small applied field, that gets larger on cooling, and changes in character on cooling through the Sm2→Sm3 phase transition at 99 °C, where it broadens. Reproduced from Sreenilayam et al[20].

The phase of interest, $\text{Sm}(\text{CP})_\alpha$ occurs in the temperature range 110 °C to 99 °C. There is a clear change in the field-behaviour of the biaxiality at the Sm2→Sm3 transition temperature. However, because these phases are tilted the authors original interpretation of the data needs to be revisited.

For our purposes, we can use these textures to distinguish the $\text{Sm}(\text{CP})_\alpha$ phase from the closely related SmCPA phase. The SmCPA phase should be weakly biaxial in homeotropic cells. The anticlinic structure should ‘average’ out any anisotropy in the dielectric tensor due to the tilt of the

molecule, but because these are bent-core phases, there is a built in anisotropy of the dielectric tensor due to the rotation symmetry breaking of the bananna structure, which should manifest in homeotropic cells as a schlieren texture that allows for $\pm 1/2$ defects.

From [Figure 2.5](#), it is clear that, for the temperature ranges of $\text{Sm}(\text{CP})_\alpha$ the textures appear dark— they have no measurable biaxiality. This means that the inherent anisotropy of the dielectric tensor of the molecule *must* be organized in a structure that averages it out. This is a clue to the helical nature of the $\text{Sm}(\text{CP})_\alpha$.

2.2.3 Electro-Optic Behaviour of the $\text{Sm}(\text{CP})_\alpha$ phase

We can study the electro-optic behaviour of PAL30 in both homeotropic and planar aligned cells. In homeotropic, you are studying the *biaxiality* of the phase, ie. the birefringence $\delta n = n_2 - n_3$. In planar aligned cells, you are studying the birefringence between the molecules long axis and some weighted combination of n_2 and n_3 that depends on the orientation.

There are two categories of behaviour you can track to get information about the phase: the polarization current and the bifrefringence/biaxiality.

2.2.3.1 Polarization Current

The $\text{Sm}(\text{CP})_\alpha$ phase manifests a slight ferrielectric behaviour, where three peaks are visible under a high resolution polarization current trace. Broadly, the phase appears to have two main peaks, usually associated with antiferroelectric behaviour.

However, the differences between these two phases becomes apparent under the application of an electric field. This is because the sequence of intermediate phases between a $\text{SmC}_\text{A}P_\text{A} \rightarrow \text{SmC}_\text{S}P_\text{F}$ is different from $\text{Sm}(\text{CP})_\alpha \rightarrow \text{SmC}_\text{S}P_\text{F}$. If the bent-core $\text{Sm}(\text{CP})_\alpha$ phase behaves like its calamitic cousin, the SmC^*_α , then under application of a field perpendicular to the helical axis, the helix of the $\text{Sm}(\text{CP})_\alpha$ distorts. This helical distortion is likely causing the three peaks visible in [Figure 2.7](#)

A more conventional series of traces for the polarization current is shown in [Figure 2.6](#), where the current is plotted as a function of time. The same data is shown in [Figure 2.7](#), where the current

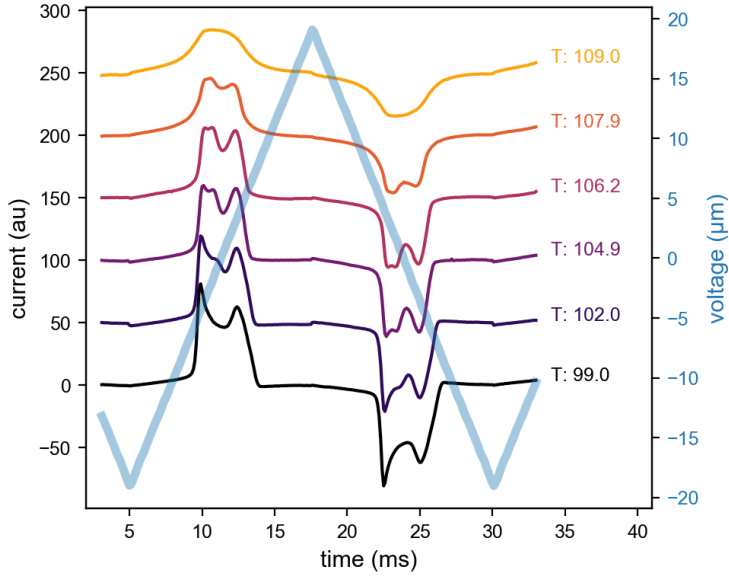


Figure 2.6: Series of polarization current measurements taken in the Sm2 phase of PAL30

is plotted directly against the applied voltage.

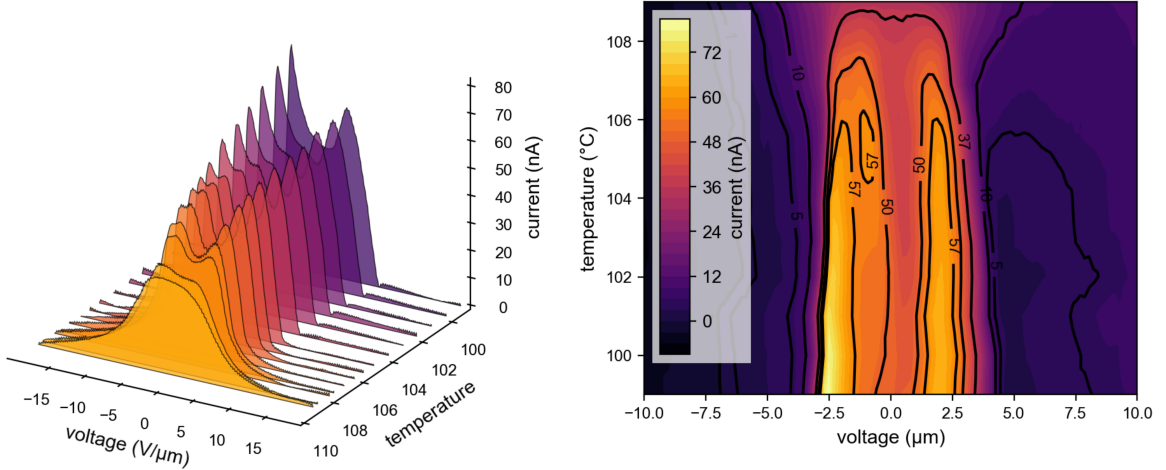


Figure 2.7: Polarization current of Sm2 of PAL30 plotted against applied voltage

A more conventional series of traces for the polarization current is shown in [Figure 2.6](#), where the current is plotted as a function of time. The same data is shown in [Figure 2.7](#), where the current is plotted directly against the applied voltage. The

2.2.4 Freely-Suspended Films of the $\text{Sm}(\text{CP})_\alpha$ phase

2.2.5 X-ray Analysis of the $\text{Sm}(\text{CP})_\alpha$ phase

The two techniques used to characterize the $\text{Sm}(\text{CP})_\alpha$ phase were SAXS (small angle hard x-ray scattering) and RSoXS (resonant soft x-ray scattering). As the SAXS is sensitive to periodicity in electron density, we can directly measure the smectic layer size (d), as shown in [Figure 2.8](#).

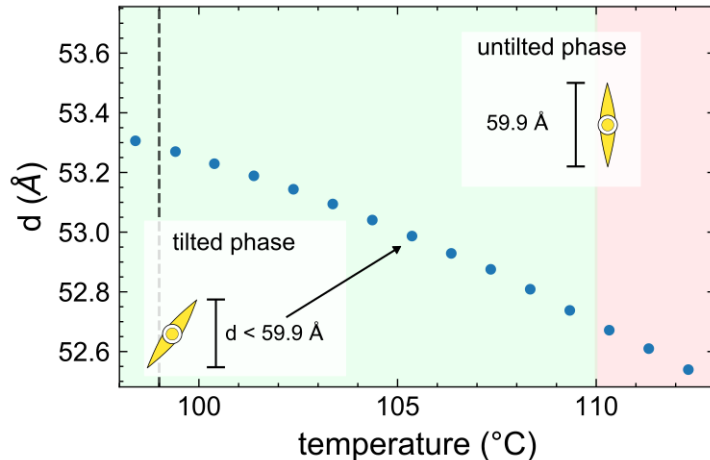


Figure 2.8: SAXS of $\text{Sm}(\text{CP})_\alpha$. The smectic layer size, d , increases monotonically on cooling, with no inflection points that would be characteristic of a untilted \rightarrow tilted phase transition.

The smectic layer size is measurably smaller than the length of an extended molecule, which supports the classification of $\text{Sm}(\text{CP})_\alpha$ as a tilted phase. However, the increase seen on cooling, which stands in contrast to the majority of bent-core materials, may indicate a significant amount of intercalation at higher temperatures.

The x-ray analysis can be greatly supplemented with the addition of resonant scattering, which is sensitive to periodicity in orientation. A resonant diffractogram taken at 104 °C is shown in [Figure 2.9](#).

By azimuthally averaging diffractograms like the one in [Figure 2.9](#) and plotting them as a function of temperature, [Figure 2.10](#), the behaviour of the $\text{Sm}(\text{CP})_\alpha$ phase can be determined over its entire temperature range.

The resonant peak corresponding to the $\text{Sm}(\text{CP})_\alpha$ phase ($d \approx 150 \text{ \AA}$) shows that this phase

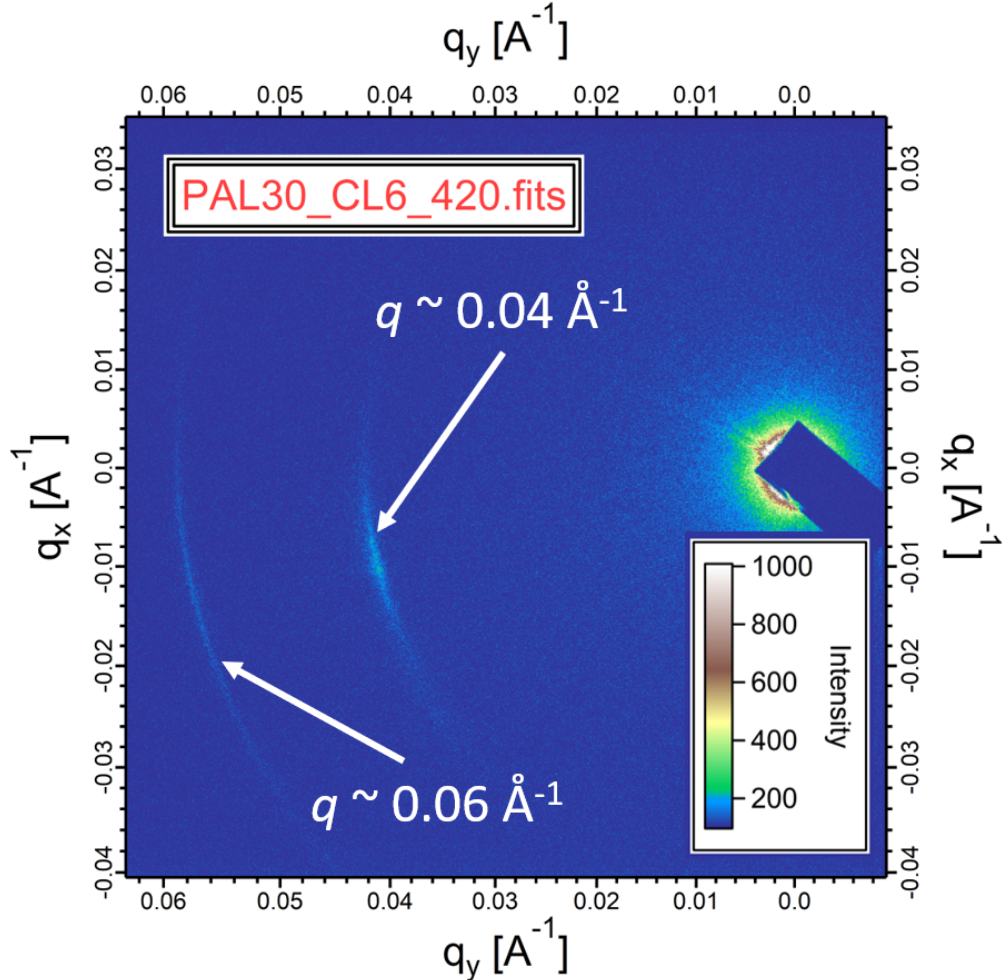


Figure 2.9: Diffractogram of PAL30 taken in the coexistence region between the $\text{Sm}(\text{CP})_\alpha$ ($q \approx 0.04/\text{\AA}$) and the SmCPA ($q \approx 0.06/\text{\AA}$).

cannot be a B2 phase (as those only have one or two layer unit-cells. However, the fact that this feature appears at roughly three times the smectic layer spacing is necessary but not sufficient for a helix. An example of this type of structure would be the proposed devil-staircase model put forth to explain a similar phase in SmC^* phase family of calamitics.

Though a detailed examination of the unit-cell structure of the $\text{Sm}(\text{CP})_\alpha$ will have to wait on the advent of polarization-resolved resonant x-ray on the carbon K-edge, we can actually confirm the helical nature of the $\text{Sm}(\text{CP})_\alpha$ phase through careful analysis.

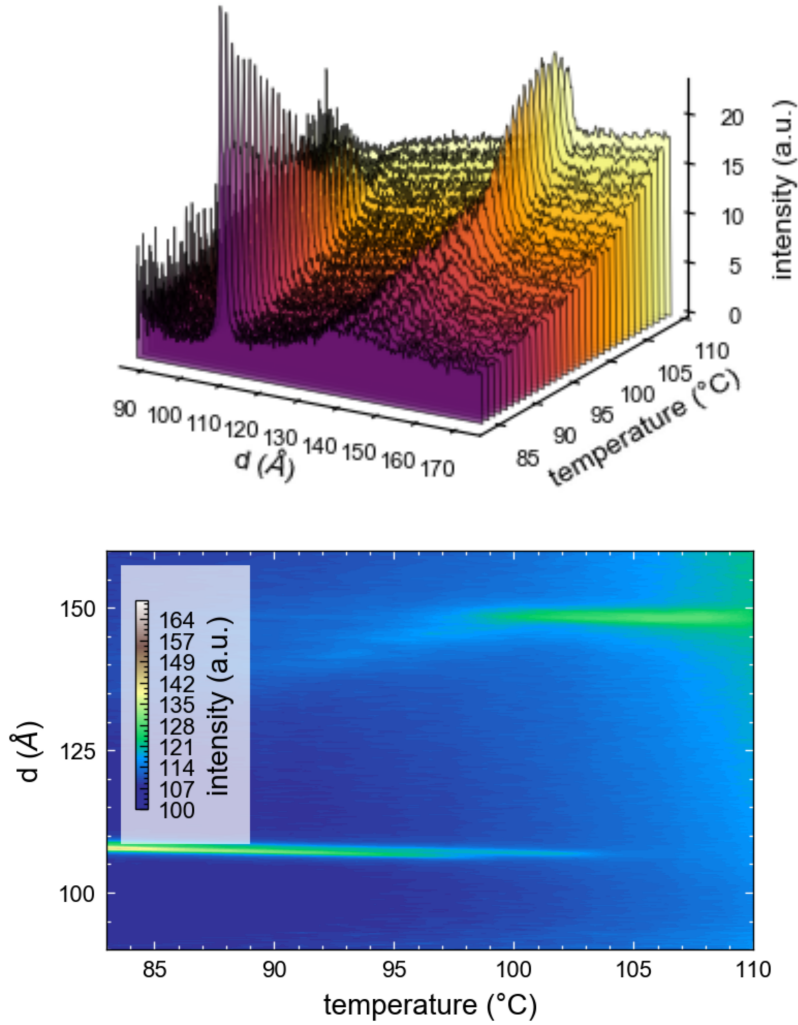


Figure 2.10: Temperature behaviour of the $\text{Sm}(\text{CP})_{\alpha}$ phase plotted as a waterfall plot in (a), and as a contour plot in (b). A bilayer ($d = 112 \text{ \AA} = 2d_0$) corresponds to the 2-layer unit-cell structure of the SmCPA phase, which sits directly below the $\text{Sm}(\text{CP})_{\alpha}$ phase in temperature. The resonant peak corresponding to the $\text{Sm}(\text{CP})_{\alpha}$ phase at $d \approx 150 \text{ \AA}$ is direct evidence that the $\text{Sm}(\text{CP})_{\alpha}$ phase is not a classic B2-type phase.

2.2.5.1 Umklapp Peaks

Though a detailed examination of the unit-cell structure of the $\text{Sm}(\text{CP})_{\alpha}$ will have to wait on the advent of polarization-resolved resonant x-ray on the carbon K-edge, we can actually confirm the helical nature of the $\text{Sm}(\text{CP})_{\alpha}$ phase through careful analysis. By combining the SAXS data

and the RSoXS data, we can deduce two things. First, that the resonant feature of the $\text{Sm}(\text{CP})_\alpha$ phase is incommensurate with the underlying smectic layer spacing. Specifically, it has a unit cell thickness of $148 \text{ \AA} \approx 2.8d_0$. Second, that we are missing an expected umklapp (harmonic) peak.

Umklapp is a german word meaning flip-over, and it refers to higher harmonics that are wrapped back into the Brioullon zone. Following Levulet and Pansu [8], where the smectic layers are modeled as stacked tensorial slabs, the master equation that predicts these flip-over harmonics is given by:

$$\frac{q}{q_0} = 2\pi l + 2\pi m \frac{1}{p}, \quad \forall l \in \mathbb{N}, \quad \forall m \in \mathbb{Z} \quad (2.5)$$

where q is the location of the expected harmonic, q_0 is the scattering off the smectic layer spacing, p is the pitch (in units of the smectic layer spacing) of the unit-cell, l is a positive integer, and m is a positive or negative integer.

From Equation 2.5, we can see one of the nearest harmonics should occur at $l = 1, m = -1$. For the $\text{Sm}(\text{CP})_\alpha$ phase, with a pitch of $p = 1/2.8$, we would expect to see a harmonic at $q/q_0 = 2\pi(1) + 2\pi(-1)\frac{1}{2.8}$. To highlight this analysis, we plot the azimuthally-averaged diffractogram in the co-existence region between the $\text{Sm}(\text{CP})_\alpha$ and the $\text{SmC}_A P_A$, on a q -scale normalized by the scattering from the smectic layer spacing, q_0 , in Figure 2.11.

include
this num-
ber

2.3 Discussion of the $\text{Sm}(\text{CP})_\alpha$ phase

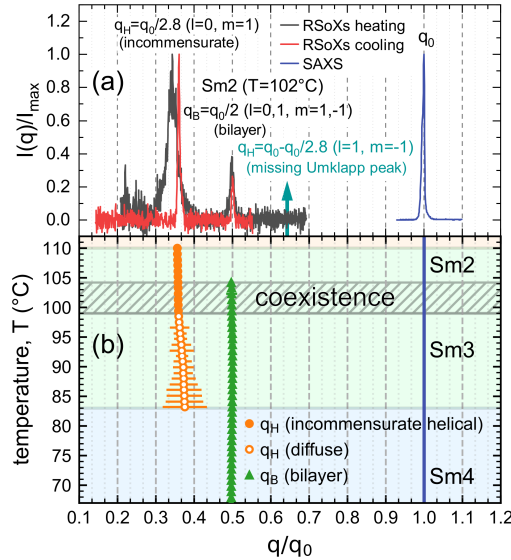


Figure 2.11: X-ray scattering from PAL30. (a) SAXS gives a peak from the smectic layer ordering at $q = q_0$. The RSoXS peak at q_H indicates that there is superlayer orientational ordering with periodicity d_H in the Sm2 phase. In general, superlayer orientational modulation in a smectic generates RSoXS peaks at wavevectors along the layer normal at $q(l, m) = l(2\pi/d_0) \pm m(2\pi/d_H)$ [8]. The observation of an RSoXS reflection at $q = q(0, 1)$ and the absence of an Umklapp peak at $q = q(1, -1)$ in the Sm2 confirms a superlayer helix with a scattering amplitude modulation due to the smectic layering that is undetectably weak. (b) Temperature dependence of resonant scattering. The helix peak at $q_H \approx 1/(2.8d_0)$ becomes diffuse in the Sm3 phase. Splitting of the bilayer peak at q_B , which would indicate helical precession of the bilayer structure, is not observed.

Chapter 3

chirality on demand: the discovery of activated Chirality in ahiral bent-core mesogens

3.1 A history of de Vries phases in liquid crystals

3.2 Characteristic behaviour of the bent-core de Vries phase

3.2.1 Textures of bent-code de Vries phase

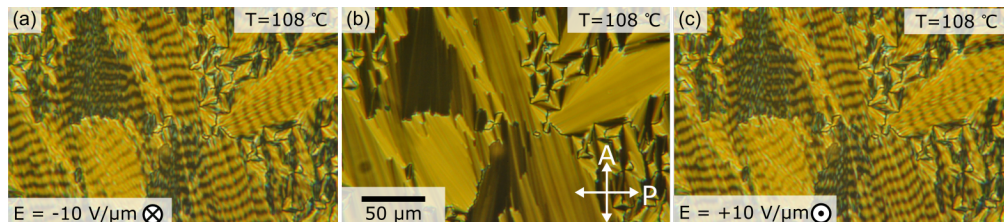


Figure 3.1:

3.2.2 Electro-optics of bent-core de Vries phase

text text

text

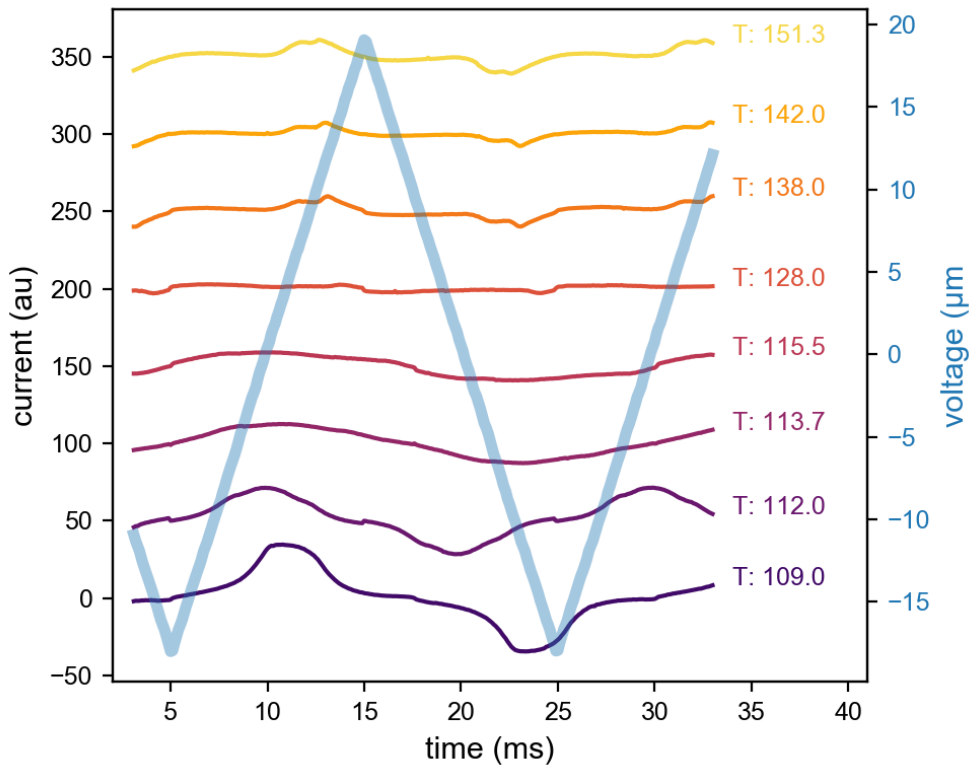


Figure 3.2:

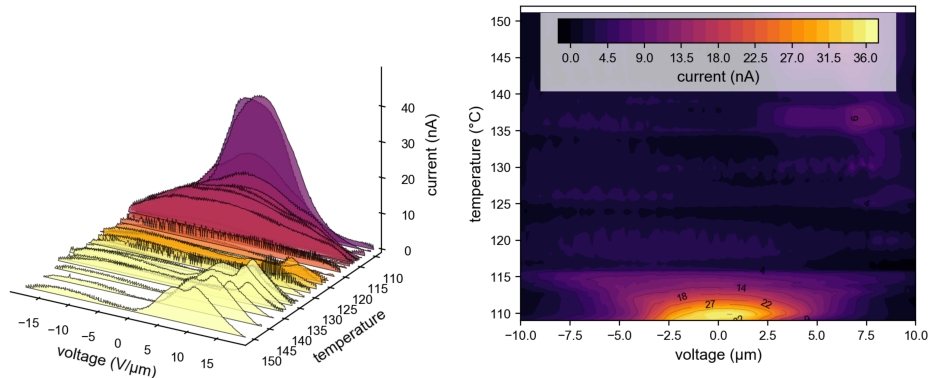


Figure 3.3:

3.2.3 X-ray analysis of bent-core de Vries phase

3.3 Discussion for the bent-core de Vries phase

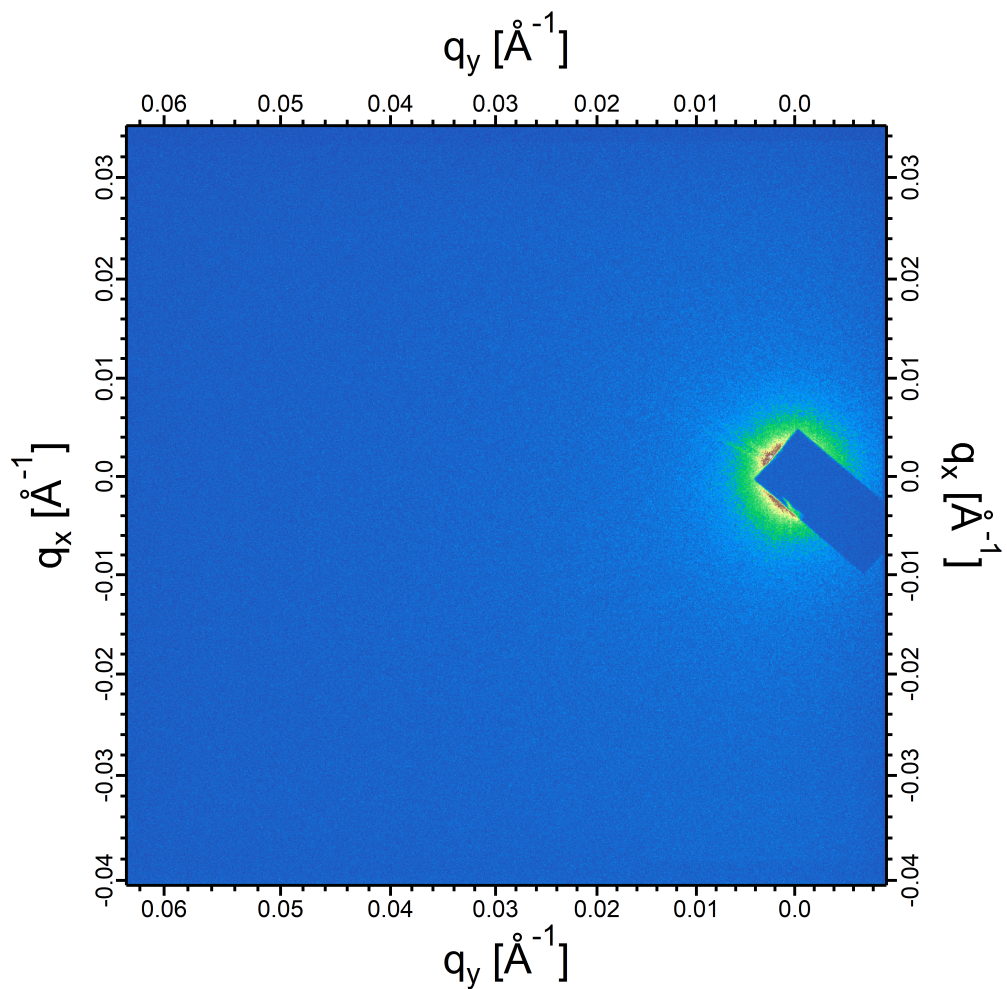


Figure 3.4:

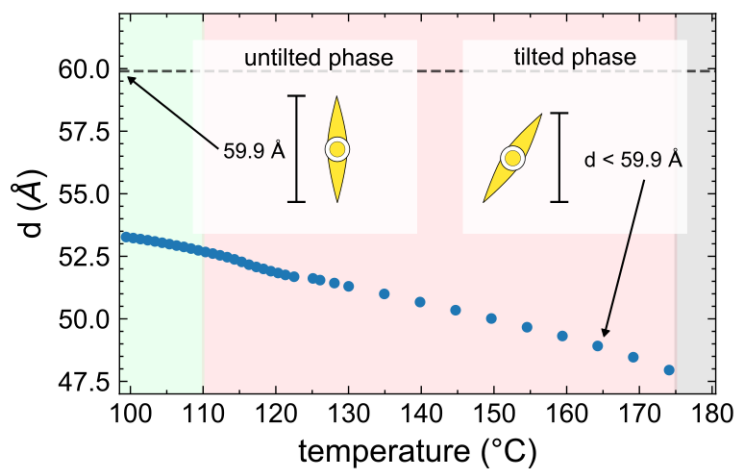


Figure 3.5:

Chapter 4

Metrology Applications of Fluid Crystals

4.1 Experimental Design

We created freely-suspended smectic films with racetrack geometry, as shown in Fig. 4.1, using 8CB (*4-n*-octylcyanobiphenyl), a fluid smectic A liquid crystal at room temperature that can be drawn into molecularly thin films freely suspended in air [25, 19, 13]. A mechanical drawing of the film holder is in the Supplemental Information.

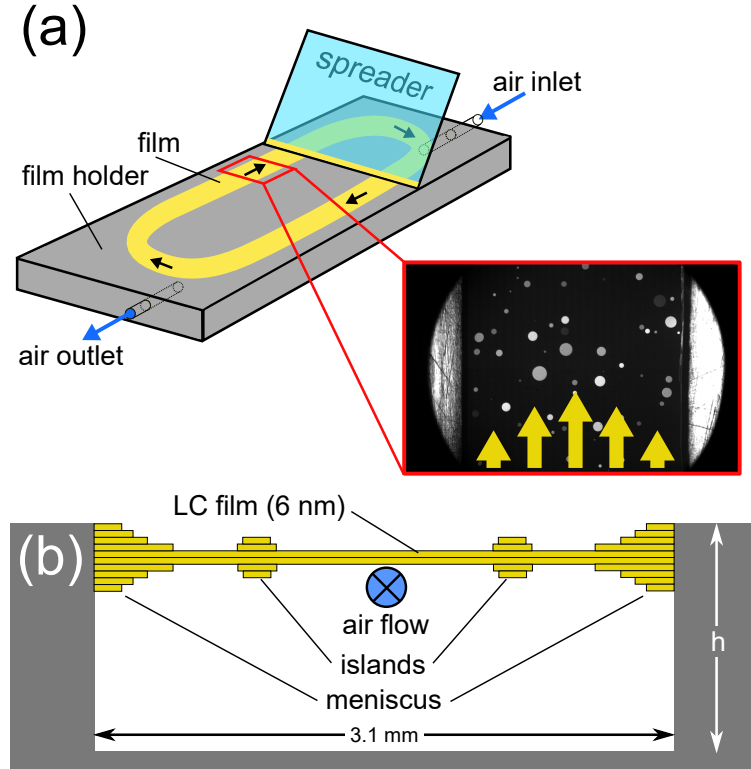


Figure 4.1: Smectic film flow meter geometry. (a) A stainless steel film holder ($45.2\text{ mm} \times 34.8\text{ mm} \times 7.6\text{ mm}$) has a $w = 3.1\text{ mm}$ -wide channel in the form of a racetrack cut to a depth $h = 3.7\text{ mm}$. At viewing ports centered along each ‘arm’, the channel is cut all the way through the film holder (a depth of 7.6 mm). Gas is coupled into and out of the system by means of co-linear, 2 mm -diameter holes at the ends of the film holder. Smectic films are created by coating the bottom of a glass coverslip (the spreader) with liquid crystal material and drawing it across the top opening of the channel. The film is shielded from random air currents from above by a sealed cover (not shown). The photomicrograph shows typical islands (localized regions with more layers than the background film) used to track flow of the film in one of the viewing regions of the racetrack. (b) Schematic cross-section of a smectic film suspended across the channel (not to scale). The film comprises an integer number of smectic layers and can be as thin as two molecules ($\sim 6\text{ nm}$). In general, a meniscus forms where the film contacts the edges of the channel.

Freely-suspended films are ideal flow sensors for several reasons. Because they are so thin, they extract very little energy from the gas jet being measured. A comparison of the effective areal

densities in our system assuming mass densities $\rho_{LC} = 1.008 \times 10^3 \text{ kg/m}^3$ and $\rho_{air} = 1.225 \text{ kg/m}^3$, and thicknesses 6 nm and 1 cm of the LC film and of the layer of air in the channel respectively, shows that the mass per unit area of the film is about 2000 times smaller than that of the air it is measuring, implying that smectic films should be very sensitive to the velocity of air flowing over them. Smectic films are intrinsically much more stable than films of conventional fluids, lasting up to several years in the laboratory, and have been used previously to probe 2D hydrodynamics [15, 7] and rheology [14], shear-stress measurements [11], and in pressure metrology [12, 24]. The application described here uses smectic films for flow measurements.

When a film is first drawn, it is typically only a few smectic layers thick and appears uniformly black in reflected light. In the prototype racetrack geometry sketched in Fig. 4.1(a), air is then injected at a known volumetric flow rate into the continuous rectangular channel located beneath the film. The inlet airflow is independently monitored using a mass airflow sensor (Honeywell AWM5101VN) capable of measuring flow rates between 0 and 5 standard litres per minute (SLPM). As the air flows through the channel, it shear couples to the liquid crystal, causing circulation of the film around the racetrack. This flow typically pulls some additional LC material in from the meniscus, leading to the formation of small, disc-like islands embedded in the film. Since the reflectance of thin, freely-suspended films depends quadratically on thickness[18], the islands are brighter than the background film and can easily be visualized using video microscopy. The motion of the islands is observed on the “backstretch” of the racetrack using a $5\times$ objective and captured using a high-speed video camera (Vision Research Phantom v12.1) at rates of 100–5000 frames per second. The islands are tracked using the open source Python library Trackpy [3], allowing us to use PTV methods [4, 1, 2, 16] to measure the velocity field of the film in the region of interest.

The device works by optically measuring the island velocity, which should be linearly coupled to the velocity of the airflow. In contrast to other mechanical flow meters, our flow meter should thus be uniformly sensitive to airflow, regardless of the airflow velocity.

Our experimental approach has much in common with traditional PTV methods, where tracer particles are injected into the gas being measured and a light sheet created by a laser is used to

define an illuminated plane, so that the tracer particles intersecting this plane can be tracked with a camera, mapping out the gas flow. A key difference is that our tracer particles (the islands) are embedded in a fluid with low vapor pressure ($< 10^{-6}$ torr)[?] that couples hydrodynamically to the gas flow, rather than relying on solid particles introduced into the gas. In the LC flow meter, the gas thus remains free of foreign tracer particles, making this a useful, non-invasive approach for systems where maintaining gas purity is important.

4.2 Theory and Simulation

In order to act as an ideal mechanical flow meter, the LC device should couple linearly to the gas flow (i.e., with a sensitivity independent of flow velocity) while having a minimal effect on the system being measured.

Linearity is an intrinsic feature of this system because of the standard no-slip boundary condition between two fluids in contact. Because the velocity of the air varies over the height of the channel, the average air and film velocities will be slightly different.

In order to model the behavior of the LC flow meter, we first consider two-phase, stratified flow in an infinitely long, rectangular pipe with symmetry about the midplane, a geometry that is amenable to an analytic approach [5, 6].

The symmetric rectangular pipe has the essential elements of the racetrack flow meter, a multiphase system where a thin fluid is surrounded by air, but has none of the complicating geometrical factors, allowing us to focus on the intrinsic properties of the air and film interaction. By varying the relative volume of the air and liquid phases (the phase fraction), we can estimate the effect of a fluid with the same thickness as a freely suspended film on the airflow.

We solved the Navier-Stokes equations to determine the airflow in the pipe both with and without the LC film, using appropriate viscosities for the air (1.8×10^{-5} Pas) and LC film (5.2×10^{-2} Pas)[?]. At values of the phase fraction corresponding to the experiment (with a thick LC film of 60 molecular layers, $\phi \sim 10^{-5}$), the flow of the LC film is found to be coupled identically

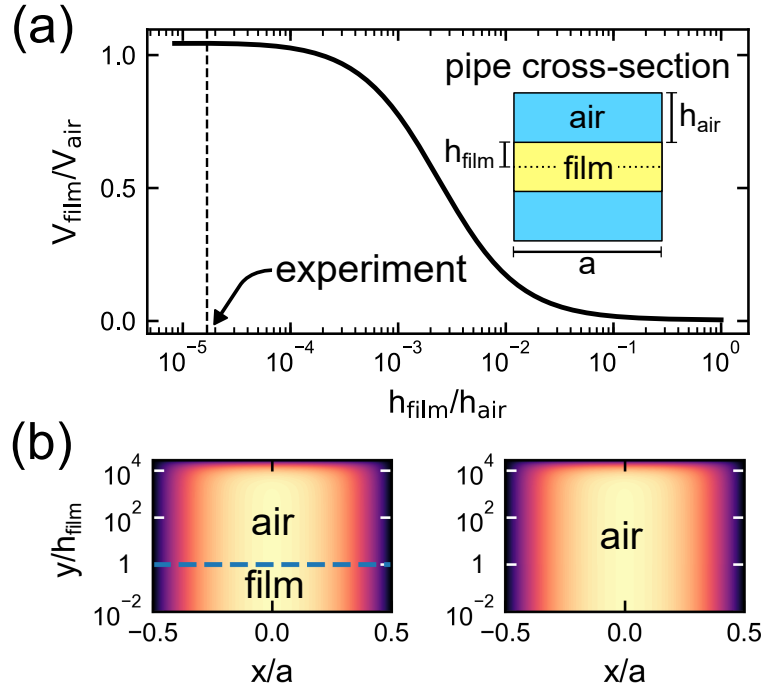


Figure 4.2: Analytic analysis of symmetric, two-phase, stratified fluid flow in an infinitely long pipe of width a . (a) Ratio between the average film and air velocities as a function of the phase fraction (the ratio of the volume of the fluid and the volume of the air, $\phi = h_{\text{film}}/h_{\text{air}}$). When the phase fraction is very small, the film is strongly coupled to the air and moves with the same speed. (b) Flow velocity in the top half of the pipe. At left, both air and film are flowing through the pipe (the blue dashed line demarcates the upper boundary of the film), while on the right only air is present. The y dimension is scaled by the half the thickness of the LC film, h_{film} . The flow fields in these two cases are practically indistinguishable, suggesting that the influence of the LC film on the airflow is negligible.

to that of the air (Fig. 4.2(a)). Furthermore, the air flow in the presence of the LC film is essentially indistinguishable from the flow in the absence of the film (Fig. 4.2(b)), suggesting that, at least in this idealized geometry, the film extracts a negligible amount of energy from the air flow. Details of these calculations are given in the Supplemental Information.

We numerically modeled the flow of air in the 3D racetrack geometry, without the liquid crystal film but choosing track dimensions and flow parameters consistent with our experiments.

Modeling the air flow alone allows us to see the “natural state” of flow in the racetrack geometry in the absence of the LC film. As the results of the analytical modeling in the previous section suggest that the film has a negligible influence on the airflow, we expect these airflow-only simulations to

closely mimic the experimental behaviour.

The results of these simulations then allow us to see whether the geometry of the racetrack modifies the linear sensitivity predicted from the analytical model. We can also test the assumption that the film has a negligible impact on the overall flow behaviour by comparing the results of the air-flow simulations to the observed experimental flow behaviour.

The simulations were performed using OpenFOAM, an open-source fluid dynamics solver that uses a SIMPLE algorithm[23]. The results are summarized in Fig. 4.3 with further details given in the Supplemental Information. The simulations indicate that at low inlet velocity values ($\lesssim 0.55$ m/s) the air stream in the channel splits, so that it flows in the same absolute direction along both arms of the racetrack. At $v_{in} = 0.55$ m/s, the airflow is predicted to transition to homogeneous, clockwise circulation.

The net force on an LC film in contact with the air stream is the sum of the shear forces along the entire length of the racetrack, for which there are two main contributions: the air moving along the shortest distance from the inlet to the outlet (at speed v_2), and the air moving along the other side of the racetrack (at speed v_1). Because the LC film is incompressible, if v_1 and v_2 are in the same absolute direction, as in Fig. 4.3(a), then the steady state film velocity is $v_{film} \propto v_2 - v_1$. This predicted film speed is in general lower than but roughly proportional to the inlet air flow, as shown in Fig. 4.3(b).

We think that the chaotic flow we observe in the racetrack is a manifestation of the ‘split-flow’ predicted by the simulations. We hypothesize that the film acts to bias the air-film system to a circulating regime, explaining why the air-film onset to circulating flow happens at lower inlet velocities than the simulations predict for pure airflow.

In summary, the analytic and numerical models both suggest that freely-suspended LC films in racetrack geometry should make excellent flow detectors, linearly coupling to and stabilizing the air flow.

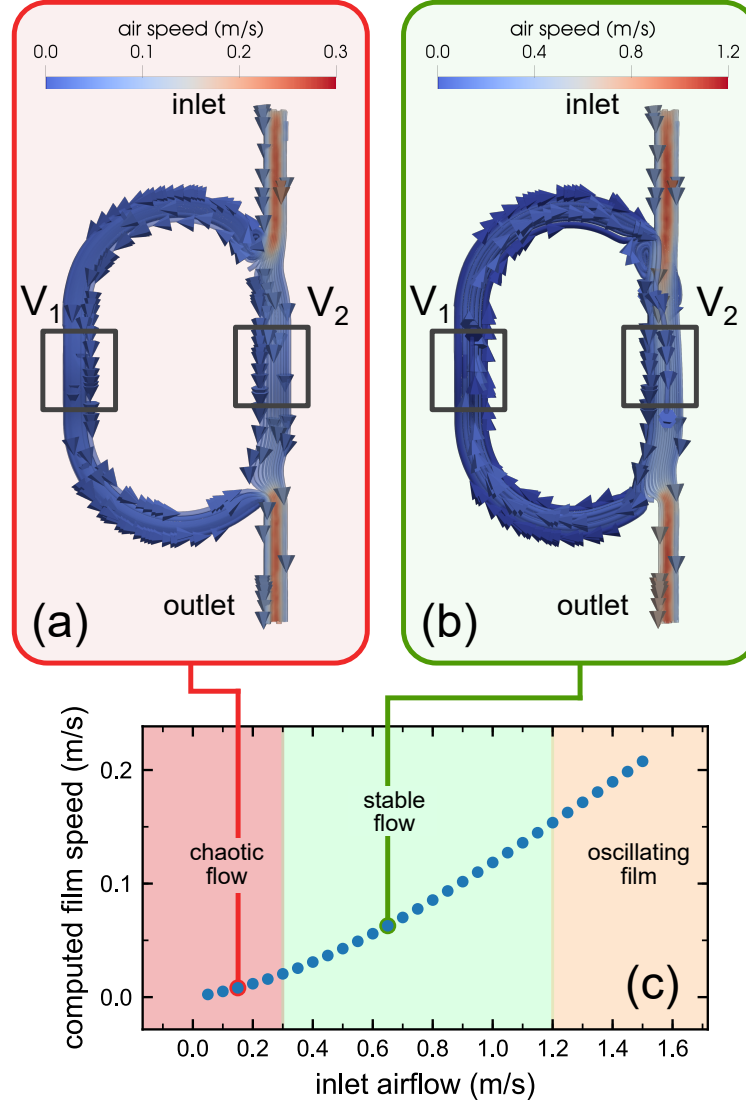


Figure 4.3: Computed airflow in the racetrack geometry. (a) Model velocity field for inlet velocity $v_{\text{inlet}} = 0.15 \text{ m/s}$. The air does not circulate uniformly in the same sense around the racetrack, instead splitting between the front and back legs. (b) Model velocity field for inlet velocity $v_{\text{inlet}} = 0.65 \text{ m/s}$. Above a transition inlet velocity of $v_{\text{inlet}} = 0.55 \text{ m/s}$, the air circulates uniformly around the racetrack. (c) Predicted net film speed ($v_{\text{film}} \propto v_2 - v_1$) for a range of inlet velocities. The slope of this curve gives an average theoretical sensitivity of $S = 0.15$. The background shading reflects the experimental observations with different inlet velocities: for $v_{\text{in}} < 0.3 \text{ m/s}$, the film flow is chaotic; for $0.3 \text{ m/s} < v_{\text{in}} < 1.2 \text{ m/s}$, the film exhibits stable Poiseuille flow; for $v_{\text{in}} > 1.2 \text{ m/s}$, the film undergoes rapid out-of-plane oscillations that make particle tracking impractical.

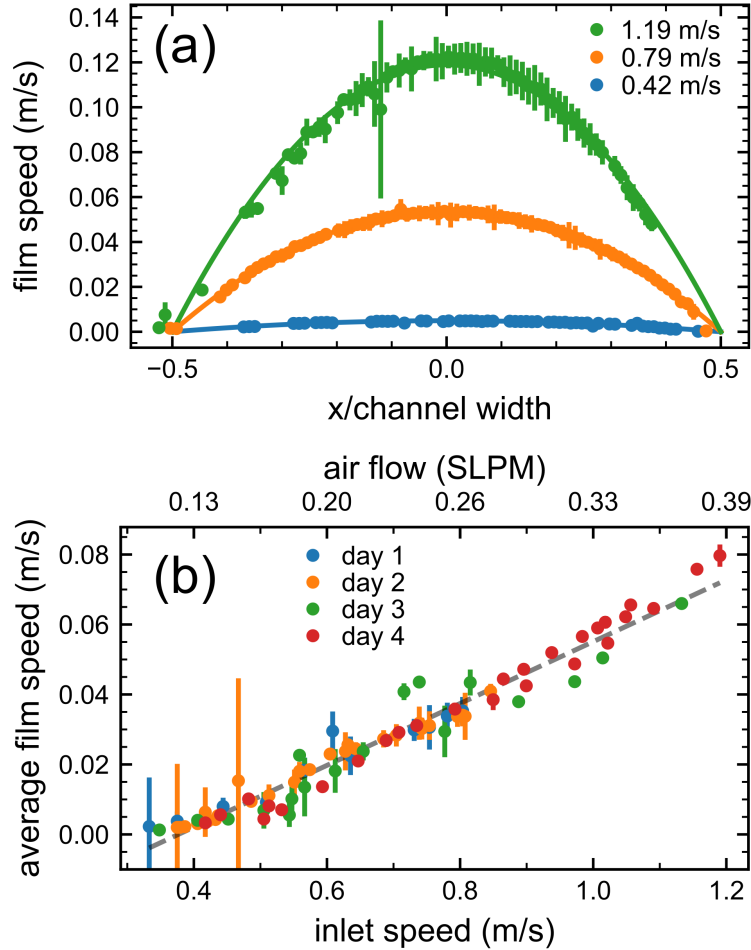


Figure 4.4: Characterization of flow meter. (a) Velocity profiles over the width of the racetrack channel, with each point corresponding to a specific tracked island. The profiles are well described by parabolas (smooth curves), confirming Poiseuille flow over a wide-range of inlet velocities. At higher velocities, the data are noisier due to the relatively paucity of islands that can be captured in sequential frames. The left-right asymmetry in the number of measurements is an artifact due to defects on one side of the camera sensor. (b) Spatially averaged film velocity in the observation region as a function of inlet air velocity. Measurements were performed over four separate days, using more than 30 films. The volumetric flow rate of the air being injected into the racetrack through the inlet was measured using an independent mechanical sensor. The average film speed is linearly proportional to the speed of the air at the device inlet, with a sensitivity that is independent of flow rate.

4.3 Results and Discussion

We measured the velocity fields of LC films coupled to inlet airflows in the range 0.1 SLPM–0.4 SLPM. We observed three main regimes of film flow behaviour, indicated by the shading in Fig. 4.3(c). Below a threshold inlet air velocity ($v_{\text{in}} < 0.3 \text{ m/s}$), the flow is characterized by time-dependent, chaotic behavior, with flow reversal and eddy currents observed in the films. This behavior is likely due to flow splitting of the type shown in Fig. 4.3(a), where the incoming air stream is divided between the short and long arms of the racetrack.

At intermediate air inlet velocities ($0.3 \text{ m/s} < v_{\text{in}} < 1.2 \text{ m/s}$), the film undergoes uniform, counter-clockwise circulation around the racetrack, as shown in Fig. 4.4(a), with a Poiseuille flow profile across the film that stabilizes in less than 1 second. The observed threshold speed for the transition from chaotic flow to uniform circulation ($v_{\text{in}} \sim 0.3 \text{ m/s}$) is somewhat lower than predicted by the simulations for airflow alone ($v_{\text{in}} \sim 0.55 \text{ m/s}$). This suggests that the film acts to stabilize homogeneous flow, promoting a uniform, regular circulation of the film and air. Because our measurement relies on obtaining regular, simple flow, the stable regime is clearly optimal for operation of the flow meter, and extending the usable range to lower inlet velocities is a clear advantage of the LC film-air system. At high air inlet velocities ($v_{\text{in}} > 1.2 \text{ m/s}$), the film oscillates rapidly up and down, causing the islands to go in and out of focus and the film eventually to break.

A comparison of the spatially averaged film speed measured half way along the back stretch of the racetrack to the independently measured inlet airflow is plotted in Fig. 4.4(b). The average slope of this graph gives a measured sensitivity of the flow meter of $S = 0.09$. This is slightly less than the sensitivity predicted from the pure airflow simulations, a difference which we attribute to air loss during the air-injection process. With some refinement of the racetrack geometry, we would expect to extend the accessible measurement range to lower velocities. The upper velocity limit could be raised by implementing measures to equalize the air pressure across the film. We believe that such differences in air pressure are responsible for the rapid vertical oscillations observed at high flow rates.

By harnessing the unique properties of freely-suspended smectic films, we have demonstrated a method for mechanical measurement of air flow that has intrinsically linear sensitivity. This technique could usefully be applied to mapping the velocity field of gases flowing through exotic microfluidic geometries in two dimensions.

Bibliography

- [1] A. A. Adamczyk and L. Rimal. 2-Dimensional particle tracking velocimetry (PTV): Technique and image processing algorithms. 6(6):373–380.
- [2] Ronald J. Adrian and Jerry Westerweel. Particle Image Velocimetry. Cambridge University Press.
- [3] Daniel B. Allan, Thomas Caswell, Nathan C. Keim, and Casper M. van der Wel. Trackpy: Trackpy v0.4.1.
- [4] Th. Dracos. Particle Tracking Velocimetry (PTV). In Th. Dracos, editor, Three-Dimensional Velocity and Vorticity Measuring and Image Analysis Techniques: Lecture Notes from the Short Course Held in Zürich, Switzerland, 3–6 September 1996, ERCOFATAC Series, pages 155–160. Springer Netherlands.
- [5] George Wheeler Govier and Khalid Aziz. The Flow of Complex Mixtures in Pipes. Society of Petroleum Engineers, 2 edition.
- [6] Dongeun Huh, Yi-Chung Tung, Hsien-Hung Wei, James B. Grotberg, Steven J. Skerlos, Katsuo Kurabayashi, and Shuichi Takayama. Use of Air-Liquid Two-Phase Flow in Hydrophobic Microfluidic Channels for Disposable Flow Cytometers. 4(2):141–149.
- [7] Tatiana Kuriabova, Thomas R. Powers, Zhiyuan Qi, Aaron Goldfain, Cheol Soo Park, Matthew A. Glaser, Joseph E. MacLennan, and Noel A. Clark. Hydrodynamic interactions in freely suspended liquid crystal films. 94(5):052701.
- [8] Anne-Marie Levelut and Brigitte Pansu. Tensorial x-ray structure factor in smectic liquid crystals. Phys. Rev. E, 60(6):6803, 1999.
- [9] Darren R. Link, Giorgio Natale, Renfan Shao, Joseph E. MacLennan, Noel A. Clark, Eva Körblova, and David M. Walba. Spontaneous Formation of Macroscopic Chiral Domains in a Fluid Smectic Phase of Achiral Molecules. Science, 278(5345):1924–1927, December 1997.
- [10] Y. P. Panarin, M. Nagaraj, S. Sreenilayam, J. K. Vij, A. Lehmann, and C. Tschierske. Sequence of four orthogonal smectic phases in an achiral bent-core liquid crystal: Evidence for the smap α phase. Phys. Rev. Lett., 107(24):247801, December 2011.
- [11] D. S. Parmar. A novel boundary layer sensor utilizing domain switching in ferroelectric liquid crystals. 62(2):474–479.

- [12] Devendra S. Parmar and Harlan K. Holmes. Pressure sensor using liquid crystals.
- [13] Ronald Pindak and David Moncton. Two-dimensional systems. 35(5):57.
- [14] Zhiyuan Qi, Kyle Ferguson, Yancey Sechrest, Tobin Munsat, Cheol Soo Park, Matthew A. Glaser, Joseph E. MacLennan, Noel A. Clark, Tatiana Kuriabova, and Thomas R. Powers. Active microrheology of smectic membranes. 95(2):022702.
- [15] Zhiyuan Qi, Zoom Hoang Nguyen, Cheol Soo Park, Matthew A. Glaser, Joseph E. MacLennan, Noel A. Clark, Tatiana Kuriabova, and Thomas R. Powers. Mutual Diffusion of Inclusions in Freely Suspended Smectic Liquid Crystal Films. 113(12):128304.
- [16] Markus Raffel, Christian E. Willert, Fulvio Scarano, Christian J. Kähler, Steve T. Wereley, and Jürgen Kompenhans. Particle Image Velocimetry: A Practical Guide. Springer.
- [17] R. Amaranatha Reddy and B. K. Sadashivaa. Influence of fluorine substituent on the mesomorphic properties of five-ring ester banana-shaped molecules. 30(9):1031–1050.
- [18] Charles Rosenblatt and Nabil M. Amer. Optical determination of smectic A layer spacing in freely suspended thin films. 36(6):432–434.
- [19] Charles Rosenblatt, Ronald Pindak, Noel A. Clark, and Robert B. Meyer. Freely Suspended Ferroelectric Liquid-Crystal Films: Absolute Measurements of Polarization, Elastic Constants, and Viscosities. 42(18):1220–1223.
- [20] S. Sreenilayam, M. Nagaraj, Y. P. Panarin, J. K. Vij, A. Lehmann, and C. Tschierske. Properties of Non-Tilted Bent-Core Orthogonal Smectic Liquid Crystal. Mol. Cryst. Liq. Cryst., 553(1):140–146, January 2012.
- [21] S. Sreenilayam, Yu. P. Panarin, J. K. Vij, A. Lehmann, and C. Tschierske. Occurrence of Five Different Orthogonal Smectic Phases in a Bent-Core (BC) Liquid Crystal. 610(1):116–121.
- [22] Sithara P. Sreenilayam, Yuri P. Panarin, Jagdish K. Vij, Vitaly P. Panov, Anne Lehmann, Marco Poppe, Marko Prehm, and Carsten Tschierske. Spontaneous helix formation in non-chiral bent-core liq. cryst. with fast linear electro-optic effect. Nat. Commun., 7:11369, May 2016.
- [23] H. G. Weller, G. Tabor, H. Jasak, and C. Fureby. A tensorial approach to computational continuum mechanics using object-oriented techniques. 12(6):620–631.
- [24] S. V. Yablonskii, K. Nakano, A. S. Mikhailov, M. Ozaki, and K. Yoshino. Pressure sensor based on freely suspended ferroelectric liquid crystal film. 80(4):571–573.
- [25] Charles Y. Young, Ronald Pindak, Noel A. Clark, and Robert B. Meyer. Light-Scattering Study of Two-Dimensional Molecular-Orientation Fluctuations in a Freely Suspended Ferroelectric Liquid-Crystal Film. 40(12):773–776.